# Experimental Study of Underexpanded Screeching Jet and Its Interaction with Upstream Reflector

David Morata*, Kyle A. Miller† and Dimitri Papamoschou.‡
*University of California, Irvine, Irvine, CA, 92697*

**The effect of a conical reflector upstream of the nozzle exit of a supersonic underexpanded jet was studied experimentally. The jet had a fully-expanded Mach number $M_j = 1.34$ and the reflector half-angle was $60°$. Experiments were performed using a near-field linear microphone array that included one continuously-scanning sensor enabling high spatial resolution. The isolated jet emitted well-known screech mode $B$ (lateral oscillation), with the fundamental tone and its harmonics appearing prominently in the sound pressure level spectrum. Addition of the reflector caused significant changes in the modal emission pattern, with new oscillation mode $E$ appearing prominently, in conjunction with mode $B$. The near-field data obtained from the continuous-scan experiments were processed using a partial fields decomposition approach, in which the fixed sensors were utilized as the phase references. The technique allowed the construction of a global cross-spectral matrix based on the finely-spaced locations of the scanning sensor. Beamforming maps and deconvolved noise source distributions were computed using the global cross-spectral matrix and provided information on the structure of the noise source for the two jets. Cross-beamforming indicated significant coherence between shock cells at the screech frequencies. The partial fields were decomposed into radiating and non-radiating components, including separation in upstream- and downstream-propagating events. This information was used to assess the location of the screech sources for modes $B$ and $E$ with a high degree of spatial resolution. Finally, the tonal partial fields were propagated to the far field using the boundary element method. The resulting directivity of the sound pressure level spectrum is in fair agreement with experimental results for the same jets**

## I. Nomenclature

| | | |
|---|---|---|
| $a$ | = | speed of sound |
| $D$ | = | jet diameter |
| $\mathbf{e}$ | = | steering vector |
| $f$ | = | cyclic frequency |
| $\mathbf{G}$ | = | Cross Spectral Matrix |
| $H$ | = | complex transpose |
| $\mathcal{L}$ | = | region of interest |
| $\mathcal{M}$ | = | number of microphones |
| $N_{\mathrm{FFT}}$ | = | size of Fast Fourier Transform |
| $p_m(t)$ | = | pressure signal of microphone $m$ |
| $P_m$ | = | Fourier transform of $p_m(t)$ |
| $\mathcal{S}$ | = | point spread function |
| $T$ | = | block length in seconds, transpose |
| $t$ | = | time |
| $U_j$ | = | fully-expanded jet velocity |
| $V$ | = | sensor speed |
| $w_m$ | = | weight of microphone $m$ |
| $x$ | = | axial coordinate |
| $y$ | = | transverse coordinate |

*Graduate Student Researcher, Mechanical and Aerospace Engineering, dmoratac@uci.edu, Member AIAA.
†Graduate Student Researcher, Mechanical and Aerospace Engineering, kamille2@uci.edu, Member AIAA.
‡Professor, Mechanical and Aerospace Engineering, dpapamos@uci.edu, Fellow AIAA.

| | | |
|---|---|---|
| $Y$ | = | noise source map |
| $\Lambda$ | = | relative shock strength |
| $\ell$ | = | source-sensor distance |
| $\theta$ | = | polar angle relative to downstream axis |
| $\mathbf{\Pi}$ | = | partial fields |
| $\sigma$ | = | singular value |
| $\mathbf{\Sigma}$ | = | singular value matrix |
| $\tau$ | = | source-sensor travel time |
| $\xi$ | = | coordinate along jet axis |
| $\omega$ | = | angular frequency |

*Subscripts*

| | | |
|---|---|---|
| $k$ | = | block index |
| $f$ | = | fixed microphone |
| $s$ | = | scanning microphone |

*Acronyms*

| | | |
|---|---|---|
| CSM | = | Cross-Spectral Matrix |
| FFT | = | Fast Fourier Transform |
| PF | = | Partial Field |
| PFD | = | Partial Fields Decomposition |
| SPL | = | Sound Pressure Level |
| XBF | = | Cross-Beamforming |

## II. Introduction

Imperfectly-expanded supersonic jets emit noise that results from turbulent mixing and the interaction of turbulent eddies with the shock-cell strusture in the jet plume. Both can be significant noise sources, so their understanding and attenuation has occupied the aeroacoustics community for several decades. Shock-associated noise contains two components: broadband shock-associated noise (BBSAN); and intense tonal emission, referred to as screech. Strong screech tones have been reported to cause damage in the aircraft structures neighboring the nozzle exit [1, 2]. Understanding the sources of screech is of fundamental importance for minimizing their detrimental effects on aircraft structures and to the health of personnel in the vicinity of such aircraft, such as on aircraft carriers.

Screech tones were first observed in the pioneering work of Powell [3], who demonstrated that screech was generated by means of a feedback mechanism loop. The flow disturbances that are generated at the nozzle lip in the form of Kelvin-Helmholtz instability waves are convected downstream and interact with the shock-cell structure of the jet. This interaction leads to acoustic waves being generated from the shock-cell tips through a mechanism known as shock leakage [4, 5]. These acoustic waves propagate downstream and upstream, with their directivity being strongly dependent on the frequency of the tone or the mode oscillation dynamics [1]. The upstream-propagating component causes the feedback loop to close, exciting the thin shear layer at the nozzle exit, and producing additional disturbances. Multiple studies have demonstrated that screech generation occurs several shock-cells downstream of the nozzle lip [6], and at multiple locations [7, 8]. Many of these past studies have used an “effective source” location from which the upstream-propagating waves appear to be generated from. As discussed by Raman [7], this is not in conflict with the phased monopole array idea of Powell if such array has an acoustic center. However, the fact that screech appears to emanate from multiple shock-cells must be appropriately determined. Mercier *et al.* [9] used near-field data and optical tools to locate the effective acoustic source of screech between the third and fourth shock cell tips for a wide range of fully-expanded jet Mach numbers. The present study utilizes near-field microphone data to construct partial fields and conduct noise source localization analysis at the screech frequency and its harmonics for two oscillation modes. The location of the shock-cells is inferred from near-field beamforming results.

Past works have demonstrated the sensitivity of screech noise dynamics on surfaces surrounding the jet nozzle. Ponton and Seiner [10] studied how the nozzle lip thickness affected the screech mode and emission characteristics on an underexpanded supersonic jet. Panda [11] studied the standing wave pattern formed in the near-field of a screeching jet. The standing wave resulted from the interaction of the downstream-propagating hydrodynamic components and the upstream-traveling acoustic waves. Based on that, he was able to derive an equation to predict the screech frequency that was dependent on the convective velocity and the wavelength of the standing wave. Raman *et al.* [12] studied the feedback loop in rectangular nozzle geometries by using circular reflectors positioned upstream of the nozzle exit. They demonstrated that the reflector changes the position of the pressure node and anti-node, thus enhancing or suppressing screech emission. The presence of upstream reflecting surfaces also causes screech cessation and reactivation [13] and screech mode switches [14]. Complex reflecting geometries such as spherical [15] or conical reflectors [16] have been also shown to change the screech emission dynamics. In particular, Morata and Papamoschou [16] showed the emergence of new screech modes caused by conical reflector surfaces near the nozzle exit. Addition of these surfaces also minimized the tonal and BBSAN emission for certain observation angles. The new mode, which they categorized as mode $E$, has not yet been described azimuthally and it is possible that it comprises an extension of a toroidal mode, the frequency of which gets reactivated with the addition of the reflector. Prediction of the screech frequency has also been a topic of intense research. For instance, Gao and Li [17] utilized the number of concurrent disturbances present at a given instance and the screech source location to predict the screech frequency for modes $A1$, $A2$, $B$, and $C$. Recent efforts using high-fidelity tools have aimed at obtaining near-field information of supersonic jet flows. Gojon and Bogey [18] studied a round underexpanded jet that contained two screech tones near mode $C$. Interest has also grown in the study of modal components of supersonic jets [19–21] for the prediction of the oscillation dynamics and screech frequency, and the study of the effects of heating [22] on supersonic jet flows.

The present work investigates the effects of a conical reflector on screech emission from an underexpanded jet using a high-resolution continuous-scan near-field microphone array. Of particular interest is the new oscillation mode $E$ that arises from installation of the reflector. A Partial Fields Decomposition (PFD) approach, in conjunction with the continuous-scan array [16, 23], is used to determine the partial fields on a radiating surface, and to obtain a global Cross-Spectral Matrix (CSM). The partial fields are then decomposed into non-radiating and radiating components, the latter being further separated into upstream- and downstream-propagating parts. This information is used to determine the location of the screech sources for modes $B$ and $E$. The noise source distribution is also obtained through a beamforming approach, and source coherence is measured using cross-beamforming (XBF). The locations of the shock-cells are determined from the beamforming results. Finally, a BEM approach is utilized to propagate the PFs to the acoustic far-field. The resulting sound pressure level spectra are compared with past experimental data.

## III. Methodology

This work utilizes a near-field microphone array that contains fixed sensors in combination with one continuously-scanning sensor. Figure 1 presents the basic layout. References [16, 24] presented a methodology for treating signals from continuously-scanning phased arrays, and Ref. [25] discussed the guidelines for an optimal signal processing. To summarize, the signal from the scanning sensor is non-stationary due to the traversing of a spatially-varying acoustic field. Non-stationarity is sought by dividing the microphone pressure signals into overlapping or non-overlapping quasi-stationary blocks, and by applying a frequency-dependent window in the computation of cross-spectral densities between microphones that have a relative velocity [24]. Among the distinct approaches that might be used to obtain the noise source distribution from continuous-scan phased arrays (e.g., direct spectral estimation [24], matrix completion [16], etc.), this work utilizes a partial fields decomposition (PFD) technique to construct a global Cross-Spectral Matrix (CSM) [16, 23]. The procedures involved in the calculation of the partial fields, construction of a global CSM, and the beamforming and XBF algorithms are described next.

### A. Partial Fields Decomposition

This section outlines the key relationships involved in decomposing the measured microphone pressure signals into partial fields on a virtual line, corresponding to the line traversed by the scanning sensor. A similar technique has been used in Refs. [16, 23] utilizing far-field measurements for sound localization purposes. The technique was originally used in the works of Lee and Bolton [26, 27] in the characterization of a subsonic jet using Near-Field Acoustic Holography (NAH).

First, a reference CSM, denoted $\mathbf{G}_{ff,T}$ is constructed as

$$\mathbf{G}_{ff,T}(\omega) = G_{f_m f_n,T}(\omega) \;=\; \overline{P_{f_m,T}(\omega)P^*_{f_n,T}(\omega)} \tag{1}$$

The matrix is constructed using the fixed sensors only, indicated by subscripts $ff$, and utilizing the complete pressure time-traces which are denoted by subscript $T$. The reference CSM has a singular value decomposition

$$\mathbf{G}_{ff,T} = \mathbf{U}_{ff,T}\mathbf{\Sigma}_{ff,T}\mathbf{V}^H_{ff,T} \tag{2}$$

where superscript $H$ is used to indicate the complex transpose. The pressure signals from all the sensors (fixed and scanning) are then divided into a number $K$ of overlapping or non-overlapping blocks. This signal division can be interpreted as generating *virtual microphones* at the geometric center of each block [16, 24]. Thus, a single scanning sensor produces $K$ virtual microphones. A transfer function matrix between the reference microphones and the continuously-scanning sensors is constructed for every block as

$$\mathbf{H}_{fs,k} = \left(\mathbf{G}_{ff,k}\right)^{-1}\mathbf{G}_{fs,k} \tag{3}$$

where $\mathbf{H}_{fs,k}$ represents the transfer function matrix for block $k$. $\mathbf{G}_{ff,k}$ is the CSM calculated utilizing the fixed sensors only for block $k$, obtained using

$$\mathbf{G}_{ff,k}(\omega) = G_{f_m f_n,k}(\omega) \;=\; \overline{P_{f_m,k}(\omega)P^*_{f_n,k}(\omega)} \tag{4}$$

and $\mathbf{G}_{fs,k}$ is the CSM obtained utilizing the fixed sensors and the scanning microphones, which is computed as

$$\mathbf{G}_{fs,k}(\omega) = G_{f_m s_n,k}(\omega) \;=\; \overline{P_{f_m,k}(\omega)P^*_{s_n,k}(\omega)} \tag{5}$$

A frequency-dependent window must be applied in the estimation of the cross-spectral densities of $\mathbf{G}_{fs,k}$ to suppress the signal non-stationarity, following the guidelines described in Ref. [24]. This work utilized the Gaussian window of Papamoschou *et al.* [24] with $c_\lambda = 0.2$ (Refs. [16, 24]) in the calculation of cross-spectral densities between microphones that had a relative velocity. The matrix $\mathbf{G}_{ff,k}$ does not necessarily have an inverse. As such, the Moore-Penrose generalized inverse (symbolized by † must be used to find an inverse matrix such that

$$\left(\mathbf{G}_{ff,k}\right)^{\dagger} = \mathbf{V}_{ff,k}\mathbf{\Sigma}^{-1}_{ff,k}\mathbf{U}^H_{ff,k} \tag{6}$$

where $\mathbf{G}_{ff,k} = \mathbf{U}_{ff,k}\mathbf{\Sigma}_{ff,k}\mathbf{V}^H_{ff,k}$ is the singular value decomposition of the matrix. The operation $\mathbf{\Sigma}^{-1}_{ff,k}$ is defined as

$$\mathbf{\Sigma}^{-1}_{ff,k} = \begin{pmatrix} \sigma^{-1}_{11} & 0 & \cdots & 0 \\ 0 & \sigma^{-1}_{22} & \cdots & 0 \\ \vdots & \vdots & \ddots & \vdots \\ 0 & 0 & \cdots & \sigma^{-1}_{\mathcal{M}_f \mathcal{M}_f} \end{pmatrix}_k \tag{7}$$

where $\sigma_{ii}$ are the ranked singular values and $\mathcal{M}_f$ is the number of fixed microphones. The partial fields for block $k$ are calculated as

$$\mathbf{\Pi}_k = \mathbf{H}^T_{fs,k}\mathbf{U}_{ff,T}\mathbf{\Sigma}^{1/2}_{ff,T} \tag{8}$$

where $T$ indicates the transpose.

### B. Beamforming

Referring to Fig. 1, a source distribution $q(\xi, t)$ is considered along the jet axis. The medium surrounding the jet is quiescent with constant speed of sound $a$. The PFD methodology outlined in the previous section is used in constructing a global CSM that enables delay-and-sum (DAS) beamforming. Following the development of Refs. [16, 23], a global CSM is obtained from the PFD as

$$\mathbf{G}_{\text{PF}} \;=\; \mathbf{\Pi}^H_i\mathbf{\Pi}_j \tag{9}$$

where $i, j = 1, ..., K$ and $\mathbf{G}_{\text{PF}}$ denotes the CSM based on the partial fields. The beamformed map is computed by steering the CSM using the traditional DAS algorithm as

$$Y(\xi, \omega) = \frac{1}{K^2}\mathbf{e}(\xi, \omega)\mathbf{G}_{\text{PF}}(\omega)\,\mathbf{e}^H(\xi, \omega) \tag{10}$$

where $\xi$ is a running coordinate along the jet axis (see Fig. 1) and $\mathbf{e}(\xi, \omega)$ is the steering vector to location $\xi$ and frequency $\omega$. The steering vector for each block $k$ is

$$e_k(\xi, \omega) = w_k \exp[i\omega_k' \tau_k(\xi)] \tag{11}$$

where $w_k$ is a weight which can include corrections for sound convected by the shear layer [28], $\omega_k'$ is a Doppler-shifted frequency that arises due to the motion of the sensor [16], and $\tau_k(\xi)$ is the source-sensor travel time from a point at location $\xi$ to the geometric center of the block $k$ (i.e., $\tau_k(\xi) = \ell_k(\xi)/a_\infty$, where $\ell_k(\xi)$ is the source-sensor distance from the block center). Here the weights were set to $w_k = 1$.

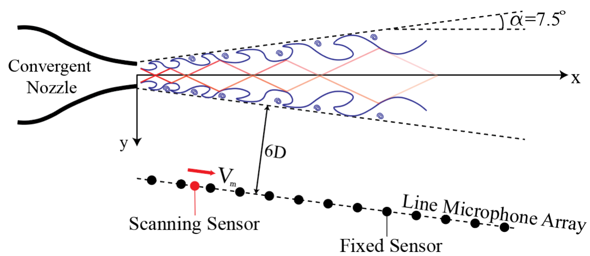


**Fig. 1 Schematic of the isolated underexpanded jet and the near-field linear array containing fixed sensors (black) and one scanning sensor (red).**

The beamformed map of Eq. 10 can be connected to the source distribution after making certain modeling assumptions. Denoting the Fourier transform of the source $q(\xi, t)$ as $Q(\xi, \omega)$, for a spatially incoherent source

$$\overline{Q(\xi, \omega)Q^*(x, \omega)} = \Phi(x, \omega)\delta(x - \xi) \tag{12}$$

where $\overline{()}$ refers to the averaging used in spectral estimation. It can then be shown that the beamformed map (Eq. 10) is a convolution between the frequency-domain source distribution $\Phi(x, \omega)$ and the array point spread function $\mathcal{S}(x, \xi, \omega)$:

$$Y(\xi, \omega) = \int_{\mathcal{L}} \mathcal{S}(x, \xi, \omega)\Phi(x, \omega)dx \tag{13}$$

where $\mathcal{L}$ is the region of interest where significant sources are expected. The points spread function (PSF) is

$$\mathcal{S}(x_0, \xi, \omega) = \sum_{m=1}^{\mathcal{M}}\sum_{n=1}^{\mathcal{M}} w_m(\xi)w_n(\xi)w_m(x_0)w_n(x_0)e^{i\omega[\tau_m(x_0)-\tau_m(\xi)]}e^{i\omega[\tau_n(\xi)-\tau_n(x_0)]} \tag{14}$$

and describes the response of the phased array to a point source at $x = x_0$. Deconvolution approaches such as DAMAS [29], Clean-SC [30, 31] or the Richardson-Lucy Bayesian estimation [16, 24] can be used to invert the convolution integral. Here the DAMAS method was selected. It was found that steering the CSM to the jet centerline or to the shear layer (Fig. 1) did not significantly change the results. As such, the region of interest has been selected on the jet centerline. It is important to note that the aforementioned beamforming approaches rely on a spatially incoherent source model (Eq. 12) and as such cannot be used to infer source coherence.

### C. Source Coherence

Traditional beamforming and deconvolution approaches assume the jet noise source to be comprised of distributed uncorrelated monopoles, as modeled in the preceding sections. However the actual source of jet noise have varying levels of coherence. Different beamforming approaches are needed to characterize acoustic sources that are partially correlated. Venkatesh *et al.* [32] proposed a new beamforming approach to address spatially-correlated sources. Harker *et al.* [33] utilized the DAMAS-C deconvolution [34] to separate the contributions of the PSF from the XBF results. They applied the method to full-scale military jet noise sources. Ravetta *et al.* [35] utilized the LORE algorithm to infer the degree of source coherence. The present study utilizes an XBF approach in conjunction with continuous-scan near-field array and the CSM constructed using Eq. 9. XBF might be considered as an extension of the traditional DAS that is able to infer source coherence. The XBF noise source map is represented as

$$Y_{\mathrm{XBF}}(\xi, x, \omega) = \frac{1}{K^2}\mathbf{e}(\xi, \omega)\mathbf{G}_{PF}(\omega)\mathbf{e}^H(x, \omega) \tag{15}$$

where the expressions for the steering vector elements are given by Eq. 11. The difference from the traditional approach is that the steering vectors are focused at different points, in this case $\xi$ and $x$. Thus $Y_{\mathrm{XBF}}(\xi, x, \omega)$ represents the estimated cross-beamforming response between locations $\xi$ and $x$ along the region of interest. The degree of source coherence between the corresponding locations is normalized relative to the individual XBF responses according to

$$\gamma(\xi, x, \omega) = \frac{Y_{\mathrm{XBF}}(\xi, x, \omega)}{\sqrt{Y_{\mathrm{XBF}}(\xi, \xi, \omega)Y_{\mathrm{XBF}}(x, x, \omega)}} \tag{16}$$

The source cross-spectral density is now defined as

$$\overline{Q(\xi, \omega)Q^*(x, \omega)} \;=\; \Phi(\xi, x, \omega) \tag{17}$$

where no assumptions with regard to the source correlation are made. It can be demonstrated that the XBF map (Eq. 15) is a convolution between the XBF point spread function and the correlated source distribution. Analogous to Section III.B, the XBF point spread function due to a source at $x_0$ takes the form

$$\mathcal{S}_{\mathrm{XBF}}(x_0, x, \xi, \omega) = \sum_{m=1}^{\mathcal{M}}\sum_{n=1}^{\mathcal{M}} w_m(x)w_n(\xi)w_m(x_0)w_n(x_0)e^{i\omega[\tau_m(x_0)-\tau_m(x)]}e^{i\omega[\tau_n(\xi)-\tau_n(x_0)]} \tag{18}$$

Deconvolution approaches [29, 36] can be applied to further sharpen the images obtained using Eq. 15. However, these methods are usually computationally demanding [37] and were outside of the scope of this study. The effects of the PSF on the XBF response were mitigated to a great extent using a block schedule that is sufficiently dense. The main lobe beamwidth of the XBF PSF has been measured to be at least 20 to 40 % wider to that of the PSF of Eq. 14, obtained assuming an uncorrelated nature about the source distribution.

### D. Radiating and Non-Radiating Components

For each frequency $\omega$, a given partial field is represented as

$$\Pi(\chi)e^{-i\omega t} \tag{19}$$

where $\chi$ is the coordinate along the path of the scanning sensor. The near-field continuous-scan array and the line traversed by the scanning sensor are schematically depicted in Fig. 1 while the partial fields are depicted in Fig. 2. The partial fields can be used as a pressure boundary condition imposed on the surface of revolution defined by the scan line from which one can propagate outwards to any field point outside the surface. If the partial fields are linear – an assumption made here – propagation involves solving the linear wave equation. The partial fields also contain information of the noise generation mechanisms and the position of the distinct acoustic sources.

Information on the propagation and radiation character of the partial field is obtained by representing $\Pi(\chi)$ in terms of its spatial Fourier transform (wavenumber spectrum) $\widehat{\Pi}(\kappa)$:

$$\Pi(\chi) \;=\; \frac{1}{2\pi}\int_{-\infty}^{\infty}\widehat{\Pi}(\kappa)e^{i\kappa\chi}d\kappa \tag{20}$$

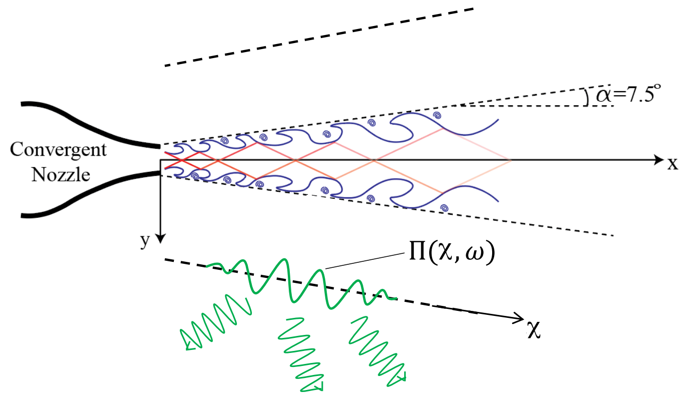


**Fig. 2 Schematic of the near-field PF concept and the radiating surface constructed by revolving the scanned region along the nozzle axis.**

where $\kappa$ is the spatial wavenumber. Combining with the $e^{-i\omega t}$ harmonic term, it is evident the part of the wavenumber spectrum with $\kappa > 0$ travels downstream and that with $\kappa < 0$ travels upstream. Importantly, the representation of Eq. 20 allows determination of the radiating and decaying components of the spectrum, which depending on the phase speed $\kappa/\omega$. The component of the spectrum with sonic or supersonic phase speeds ($|\kappa/\omega| \geq a$) radiates to the far field, while the component with subsonic phase speeds ($|\kappa/\omega| < a$) is evanescent. This can be summarized as follows:

$$| \kappa_{\text{sup}}| \leq \frac{\omega}{a}$$

$$| \kappa_{\text{sub}}| > \frac{\omega}{a}$$

where the subscripts “sup" and “sub" denote the radiating (sonic or supersonic) and decaying (subsonic) wavenumbers, respectively. The radiating component can be further separated into upstream- and downstream-propagating waves depending on the sign of $\kappa_{\text{sup}}$, as stated previously. This allows the determination of upstream- and downstream-traveling wave generation processes that constitute an essential mechanism in the jet screech feedback loop. The high spatial resolution of the microphone array enabled accurate computation of the Fourier transform $\widehat{\Pi}(\kappa)$, which in turn enabled the characterization of propagation.

### E. Boundary Element Method

In the harmonic representation of a partial field

$$p(x, y, z, t) = \Pi(x, y, z)e^{-i\omega t} \tag{21}$$

linear propagation in a quiescent medium with constant speed of sound $a$ is governed by the Helmholtz equation

$$\nabla^2\Pi + \left(\frac{\omega}{a}\right)^2 \Pi = 0 \tag{22}$$

This work employed the partial fields obtained in section III.A as a pressure boundary condition, on the radiator surface shown in Fig. 2, to solve the Helmholtz equation using the boundary element method (BEM). The Fast Multipole implementation of the BEM (FastBEM commercial code, [38]) was used to evaluate the pressure field at a number of field points, including locations where far-field measurements of the sound pressure level were available for the same jet.

## IV. Experimental Setup

### A. Jet Flow

This study examined underexpanded round jets issuing from a convergent nozzle with exit diameter $D = 14.22$ mm and lip thickness of 0.4 mm. The nozzle was supplied by air at room temperature at a total pressure $p_0 = 297$

kPa, resulting in a fully-expanded Mach number $M_j = 1.34$ and fully-expanded velocity $U_j = 397$ m/s. The Reynolds number based on nozzle exit diameter was $6.5 \times 10^5$. A conical reflector was mounted at the exit of the nozzle as depicted in Fig. 3. The reflector had a base diameter of 60.0 mm ($4.22D$) and cone half-angle of 60°. The surface was 3D printed using a Formlabs Form 2 printer, and polished so that the surface roughness was much smaller than the screech acoustic wavelength. Structures upstream of the nozzle were covered with anechoic foam to minimize any reflections towards the nozzle. The coordinates of the isolated nozzle and nozzle with deflectors are plotted in Fig. 3.

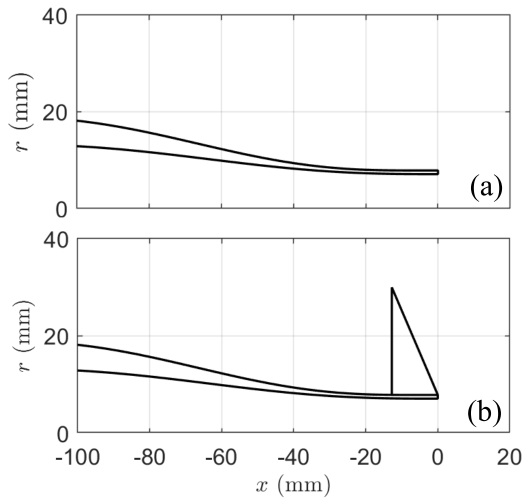


**Fig. 3 Coordinates of: (a) the isolated nozzle; and (b) nozzle with the 60° conical reflector.**

### B. Microphone Array

Noise measurements were conducted in the UCI Aeroacoustics Facility. The microphone array comprises twenty-four 1/8-inch condenser microphones (Brüel and Kjaer, Model 4138) with frequency response up to 120 kHz. The microphones are connected, in groups of four, to six conditioning amplifiers (Brüel and Kjaer, Model 2690-A-0S4). The outputs of the amplifiers are sampled simultaneously, at 200 kHz per channel, by three 8-channel multi-function data acquisition boards (National Instruments PCI-6143) installed in a computer with an Intel i7-7700K quad-core processor. National Instruments Labview software provides the interface for signal acquisition and filtering, as well as control of the experiment. The microphone signals were conditioned with a high-pass filter set at 350 Hz to remove any spurious noise. Temperature and humidity inside the chamber were recorded to enable the calculation of the effects of atmospheric absorption. The microphone array consisted of several fixed sensors in conjunction with one continuously-scanning microphone. The scanning microphone was mounted on a linear traverse consisting of a belt drive (Igus ZLW-0630) powered by a servo motor (ClearPath MCPV). The position of the scanning microphone was determined from the encoder signal of the motor powering the traverse. The servo was programmed to rotate at fixed revolutions per minute with a velocity ramp-up and ramp-down to prevent damage to the scanning microphone.

The near-field measurements were conducted with the microphones mounted on a linear inclined array in the vicinity of the jet flow. The line array was positioned approximately parallel to the jet expansion boundary with $\alpha \approx 7.5°$, and was located $6D$ away from it (Fig 1). The jet spreading rate is defined as the radial station at which the velocity is 95% of the mean flow velocity. Yüceil and M. Ötügen [39] measured the spreading of a supersonic underexpanded jet at a similar fully-expanded Mach number to be close to 5.5°. As such, the microphone array was sufficiently far from the jet to prevent damage to the microphones or interference with the jet feedback process. An image of the near-field array is shown in Fig. 4.

Two sets of experiments were performed with closely-spaced fixed microphones to capture the large-scale and small-scale acoustic emissions and the screech tones appropriately. The first set encompassed a group of 18 sensors: 17 fixed microphones positioned between $x/D = 0$ and $x/D = 15$ (Fig. 6). The scanning sensor traversed the fixed sensors at a scan speed of 13 mm/s, covering the region $x/D = 3$ to $x/D = 14$. Beamforming and XBF utilized 16 fixed sensors and the scanning microphone. The trajectory of the scanning microphone was parallel to the fixed

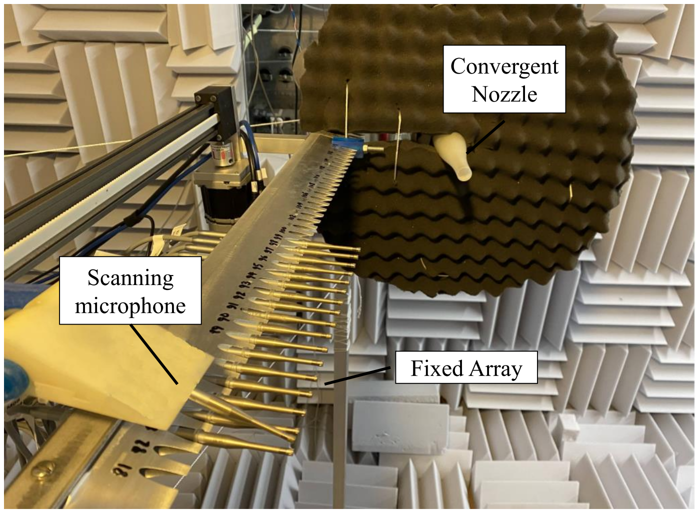


**Fig. 4 Photograph of the anechoic chamber. The near-field microphone array, including the scanning sensor, and the nozzle are marked.**

microphone line, with a lateral offset $\Delta z = -5.5$ mm. The scanned area and the positions of the fixed references are shown in Fig. 6a. This combination captured well tones $B^{(2)}$, $B^{(3)}$, and $B^{(4)}$ for the isolated jet, and $E^{(2)}$, $F^{(1)}$ and $B^{(2)}$ for the reflector configuration. The total experiment time was 18 seconds, corresponding to 3.6 $\times 10^6$ samples. Computation of the partial fields, beamforming, and XBF entailed division of the signal into 80 blocks each containing 16384 samples, corresponding to a block duration of 0.08 and travel distance of 1.1 mm. The blocks had zero overlap. The shape of the PSF at the nozzle exit ($x = 0$) is shown in Fig. 5a for reference. The PSF has been normalized for each frequency, thus the value $\mathcal{S}/\mathcal{S}_{max}$, which ranges from 0 to 1, is shown. The PSF is generally free of strong sidelobes for the frequencies of interest of this work, allowing for a high-resolution source localization. The normalized main lobe beamwidth is shown in Fig. 5b and follows the relation

$$B_{-3dB} \approx \frac{CR}{Lf}$$

where $R = 9.21D$ is a reference distance between the array center and the nozzle exit, $L = 14D$ is the array aperture and $C = 59072$ Hz is an experimentally-measured constant for the array configuration of Fig. 6a. This geometrical configuration is designed to discern sources that are at least $\sim 1D$ apart for frequencies higher than 25 kHz. The second

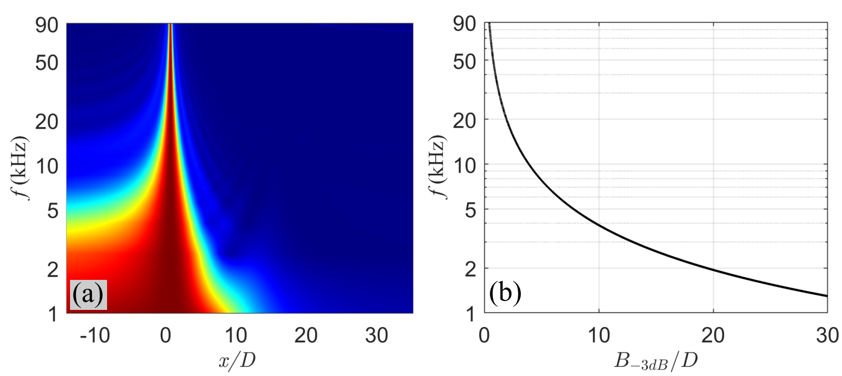


**Fig. 5 (a) Normalized PSF ($\mathcal{S}/\mathcal{S}_{max}$) at $x = 0$ as given by Eq. 14; and (b) main lobe beamwidth at $x = 0$.**

set of experiments utilized the array configuration shown in Fig. 6b. This geometrical deploymet was used to capture the behavior of tones $B^{(1)}$ for the isolated jet and $E^{(1)}$ for the reflector case. The scanning sensor traversed the fixed sensors at a scan speed of 26 mm/s, covering the region $x/D = 3$ to $x/D = 27$. The total experiment time was also 18 seconds, corresponding to 3.6 $\times 10^6$ samples. Computation of the partial fields for this case entailed division of the signal into 120 blocks each containing 16384 samples, corresponding to a block duraction of 0.08 seconds and travel distance of 2.2 mm. The blocks had zero overlap.

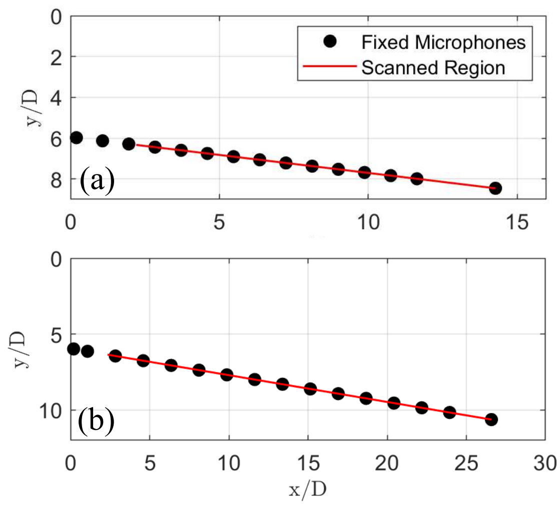


**Fig. 6 Array configurations: (a) used for frequencies higher than that of tone $E^{(1)}$; and (b) used for frequencies higher than that of tone $E^{(1)}$. Fixed microphone coordinates are indicated in black, and scanned region in red.**

## V. Results

### A. Partial Fields Decomposition

The partial fields decomposition relies on having a sufficient number of microphones to capture the distinct sources within the jet flow field. As such, construction of the CSM utilized for phase-referencing, given by Eq. 1, is of utmost importance. The singular values of $\mathbf{\Sigma}_{ff,T}$ (Eq. 2) provide an estimate of the accuracy of the partial fields decomposition technique utilized. The difference between the singular values at distinct frequencies is related to the number of independent acoustic sources present in the flow field. The odd-numbered ranked singular values for the two jet configurations are shown in Fig. 7, where the $\mathbf{\Sigma}_{ff,T}$ matrix has been obtained using the fixed sensors of the array configuration of Fig. 6a. For each configuration, the leading partial field captures practically all of the energy of the tonal components of interest here. With regards to the broadband component, there is leading PF is sufficiently separated from the other PFs up to a frequency of 60 kHz. In the following sections, only the leading PF will be analyzed. The spectra shown in Fig. 7 were computed with $N_{\mathrm{FFT}} = 1024$.

### B. Sound Pressure Level Spectra

SPL spectra are presented for fixed microphones and are based on full record of the signal acquisition (18 seconds). The spectra were computed with $N_{\mathrm{FFT}} = 4096$ yielding a frequency resolution of 49 Hz. They are plotted for several near-field positions, at which one encounters a wide variety of tones. The notation $X^{(n)}$ is used to designate a screech tone, where $X$ is the mode and $n$ is the harmonic. The mode notation of Ref. [40] is followed, with mode $B$ denoting a lateral oscillation. The jet with reflector emitted an “unknown" mode, denoted as mode $E$ in Ref [41]. Tone $F$, which appeared to arise from the interaction between two modes, appeared for the reflector configuration. Its frequency follows $f_{F^{(1)}} \approx f_{B^{(1)}} + f_{E^{(1)}}$.

Figure 8 displays the lossless SPL spectra for the isolated jet (black) and the jet with the reflector (red) for several axial locations. Tones $B^{(1)}$, $B^{(2)}$, $B^{(3)}$ and $B^{(4)}$ appear very prominently for the isolated jet. Their directivity is not uniform, hence their levels vary depending on axial station of the microphone [42, 43]. With the reflector, tones $E^{(1)}$,

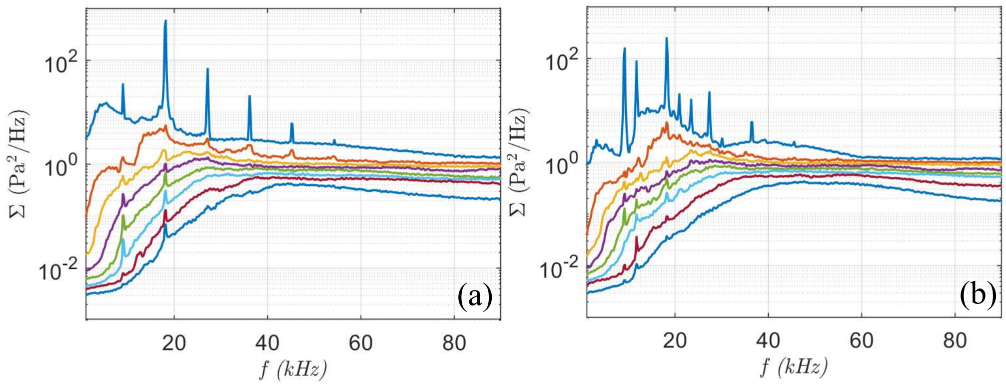


**Fig. 7 Odd-numbered ranked singular values (Eq. 2) for the isolated jet (a) and the 60° reflector case (b).**

$E^{(2)}$ and $F^{(1)}$ increase, with tone $E^{(1)}$ dominating all the surveyed positions. The reflector generally suppresses the peak tone level at the upstream-most stations and causes a decrease of the broadband shock-associated noise. It was found in Ref. [41] that modes $B$ and $E$ are coexisting, and no mode switching for the 60° configuration was discerned.

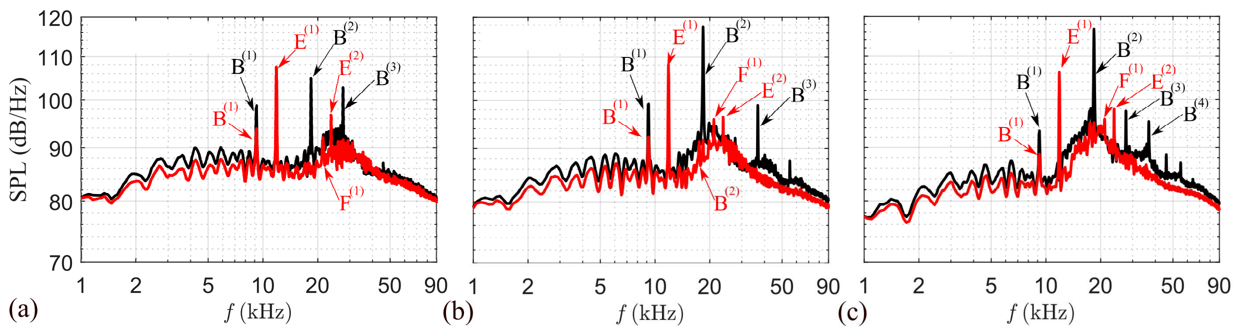


**Fig. 8 SPL spectra for the isolated jet (black) and the jet with the 60° reflector (red) at several axial stations. (a)** $x/D = 2.15$**; (b)** $x/D = 0.9$**; and (c)** $x/D = -0.8$

## C. Near-Field Beamforming

The beamforming method introduced in Section III.B allows measurement of the space-frequency distribution of the noise source with very high spatial resolution. Beamforming results for the isolated jet and the reflector configuration are shown in Figs. 9a and 9b, respectively. They were obtained with the array configuration of Fig. 6a. The array output was deconvolved using DAMAS.

Significant noise sources for the isolated jet and the reflector configuration extend up to about $13D$. For the isolated jet, intense sources near 9, 18, 27 and 36 kHz represent tones $B^{(1)}$, $B^{(2)}$, $B^{(3)}$ and $B^{(4)}$. Reflection from the nozzle lip ($x = 0$) can be distinguished for $B^{(1)}$. For the reflector configuration, intense images are seen in the region $-3D < x < 0$ for tones $B^{(1)}$ (9 kHz) and $E^{(1)}$ (12 kHz). These correspond to upstream-propagating waves from the jet screech feedback loop that are being reflected and scattered from the edge of the reflector. For the isolated jet, two vertical streaks are discernible in the frequency range $30 \leq f \leq 90$ kHz. They correspond, approximately, to the locations of the fourth and fifth shock cells of the jet. Most of the broadband shock-associated noise is produced within this narrow region of the jet For the jet with reflector, these streaks are less pronounced. Additional thin vertical streaks can be seen for $2 \leq x/D \leq 5$ for the two jet configurations. These represent the approximate location of the first, second, and third shock-cells. The geometric characteristics of shock-cells is studied next.

A new parameter, defined as the relative shock strength, is introduced to quantify the differences between the

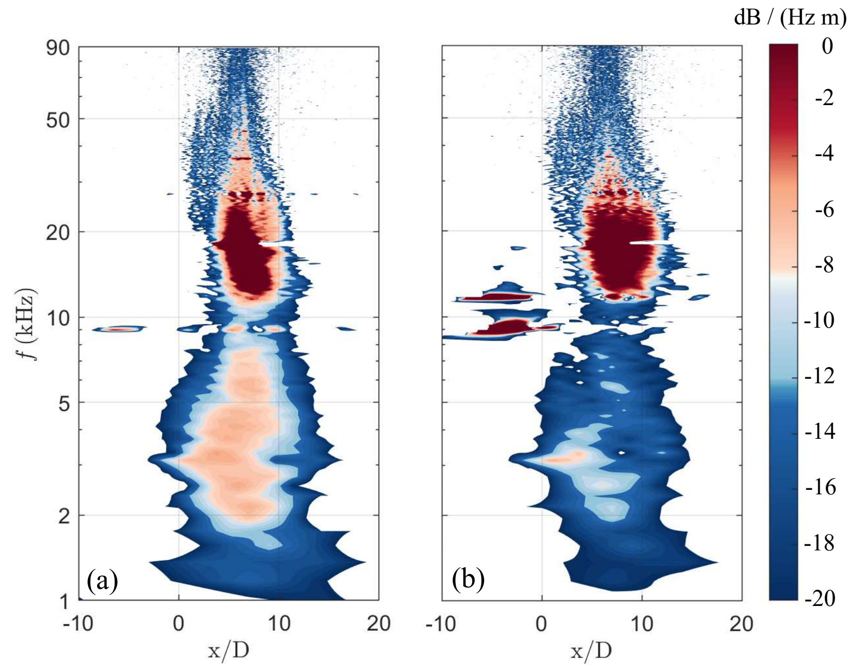


**Fig. 9 DAMAS deconvolved source distribution $\Phi(x, \omega)$. (a) Isolated jet; (b) jet with reflector.**

shock-cell patterns of two jet flow fields and determine the peak generation region. It is defined as follows:

$$\Lambda = \frac{\int_{\omega_1}^{\omega_2} \Phi(\xi, \omega) d\omega}{\max\left(\int_{\omega_1}^{\omega_2} \Phi(\xi, \omega) d\omega\right)} \tag{23}$$

where the integration in frequency is carried out to smooth the spurious wiggles of the noise source distribution. The frequency range was chosen to be from 42.7 kHz to 46.7 kHz, where one can visualize the shock-cell structure of the jet flow. The relative shock strengths for the isolated jet and the reflector case are plotted in Fig. 10 in black and red, respectively. The location of the shock sources are marked with dashed black lines and are counted in downstream order. The peak generation for the broadband shock-associated noise appears to be near $x/D = 6.6$, corresponding to the location of the fifth shock cell. The relative strength of the fourth shock source is similar for both nozzle configurations. However, the relative strengths of the first, second and third shock sources are stronger for the reflector configuration when compared to the isolated jet, exceeding 50% of the peak shock strength. With the reflector, two new peaks appear near $x/D = 0.65$ and $x/D = 7.46$ Additionally, the shock-cell spacing $s$ is approximately constant $s \approx 1.17D$ and equal for both nozzle configurations. A similar spacing was inferred from the far-field beamforming measurements of Morata and Papamoschou [16], and was measured directly, using optical means, by Mercier *et al.* [9].

### D. Source Coherence

The source coherence is studied next. It is of particular interest to visualize the degree of coherence at the screech tone frequencies near locations of peak noise generation where the interaction of the downstream-propagating disturbances and the shock-cells produce upstream-propagating waves through shock leakage [8]. The results are depicted as contour maps of $|\gamma(x, \xi)$ at specific values of the frequency $\omega$. The results for the isolated jet are displayed in Fig. 11. Contours of $|\gamma(x, \xi)$ are plotted at the frequency of tone $B^{(2)}$, frequency midway between $B^{(2)}$ and $B^{(3)}$, frequency of tone $B^{(3)}$ , and frequency midway between $B^{(3)}$ and $B^{(4)}$. Black lines denote the locations of the shock cells and follow the convention of Fig. 10. It is evident from the plots that there exists a high degree of coherence between the third, fourth and fifth shock cells for tones $B^{(2)}$ and $B^{(3)}$, clearly manifesting the oscillatory nature of the jet flow at the screech frequency and its harmonics. At the midway frequencies there is no coherence of the shock-cells.

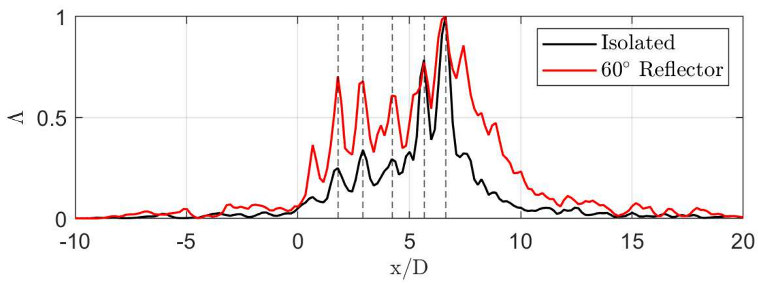


**Fig. 10 Axial distribution of relative shock strength.**

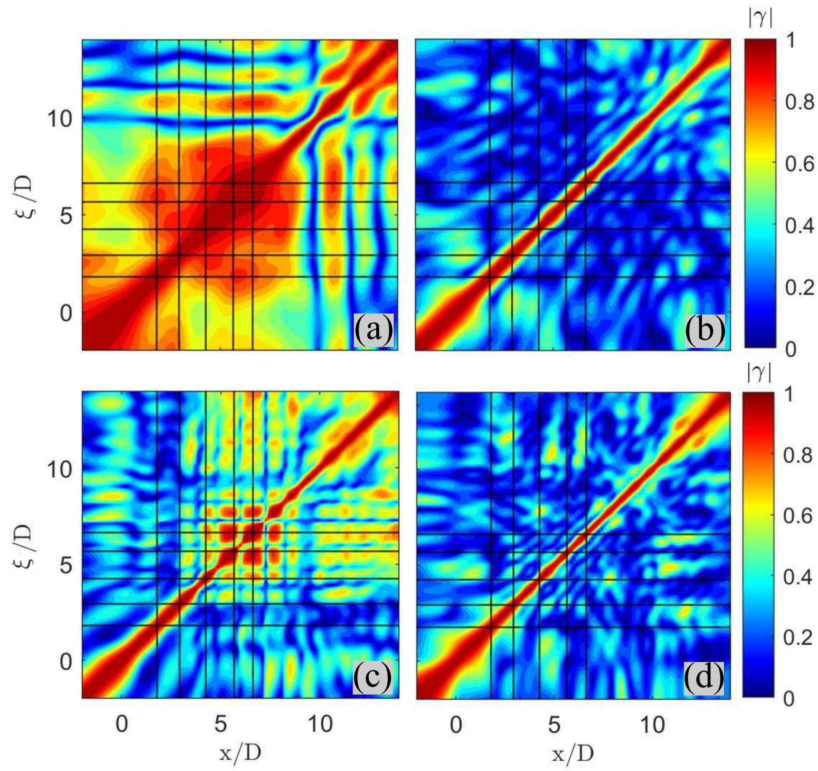


**Fig. 11 Magnitude of complex coherence for the isolated jet at frequencies: (a) tone $B^{(2)}$; (b) between $B^{(2)}$ and $B^{(3)}$; (c) tone $B^{(3)}$; and (d) between $B^{(3)}$ and $B^{(4)}$. Black lines denote the locations of shock cells.**

Additionally, it is instructive to examine the magnitude of source coherence for the broadband shock-associated noise for the same frequency range as that used to produce Fig. 10. This is done in Fig. 12. Averaging in frequency was been performed to smooth the coherence distribution. There does not appear to be any coherence between the fourth and the fifth shock-cells. However, certain degree of coherence that rapidly decays is noted around the second, third, and fourth shock cell with their surroundings. Figures 11 and 12 indicate that the shock-cells are subject to strong oscillations at the frequencies of mode *B* and its harmonics, but can be considered as incoherent sound sources at other frequencies.

The analogous results for the jet with the reflector are displayed in Fig. 13, which encompasses tones $F^{(1)}$, $E^{(2)}$, and $B^{(3)}$, and a frequency between $F^{(1)}$ and $E^{(2)}$. A certain degree of coherence is noted after the fifth shock cell for the interaction tone $F^{(1)}$. This could be related to the reinforced shock-cell structure and the presence of additional shock sources for this case when compared to the isolated jet, as seen in Fig.10. Tone $E^{(2)}$ does not show a defined pattern of coherence, in sharp contrast to tone $B^{(2)}$ for the isolated jet, which showed a widely-coherent area near the

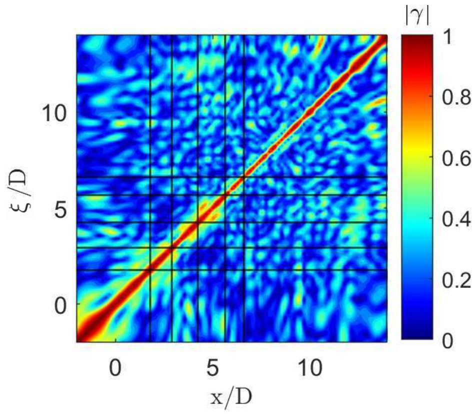


**Fig. 12 Magnitude of complex coherence for the broadband shock-associated noise of the isolated jet. Black lines denote the locations of shock cells.**

shock-cell structures. There seems to be a highly coherent pattern for tone $B^{(3)}$, in sharp contrast to the coherence plot of the isolated jet at the same frequency (Fig. 11c). The flow appears to be highly sensitive to the resonant frequency of tone $B^{(3)}$ for this case. The coherence of tone $B^{(2)}$ is similar to that shown in Fig. 11 for the isolated jet, and was not included for brevity.

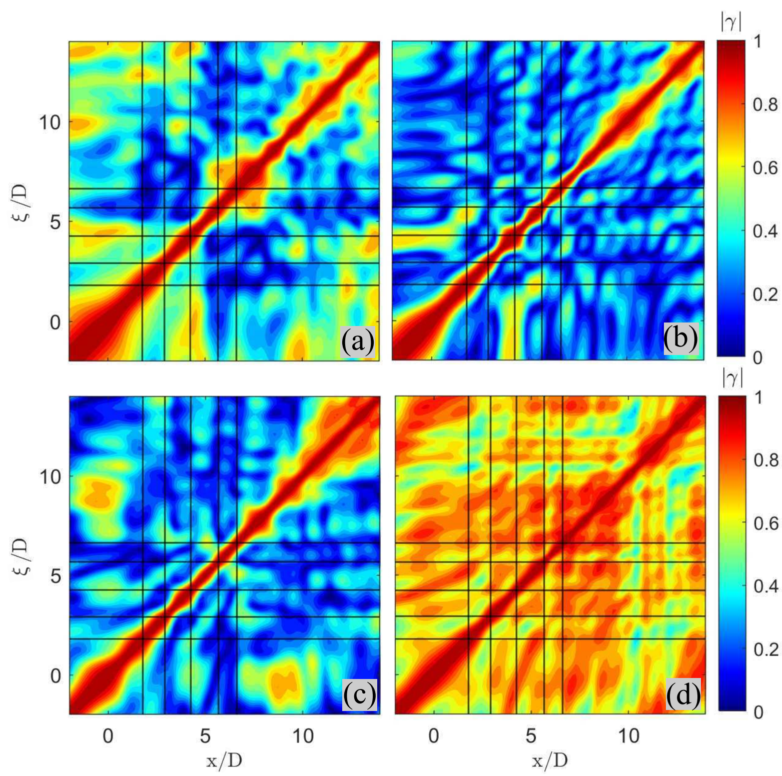


**Fig. 13 Magnitude of complex coherence for the jet with reflector at frequencies: (a) tone $F^{(1)}$; (b) tone $E^{(2)}$; (c) between $F^{(1)}$ and $E^{(2)}$ (d) tone $B^{(3)}$; and Black lines denote the locations of shock cells.**

## E. Partial Fields

The partial fields obtained using Eq. 8 have been used to produce the previous beamforming and XBF results. Besides their fundamental role in obtaining the CSM used to discern the noise source distribution, the PF can be used as a boundary condition to produce an equivalent acoustic far-field using a boundary element method (BEM) or inform a screech model. The continuous-scan approach offers superior spatial characterization of the PF without incurring exorbitant experimental costs. The PF for the isolated jet at tones $B^{(1)}$, $B^{(2)}$, and $B^{(3)}$ are plotted in Fig. 14. High amplitudes of the real or imaginary parts are associated with regions of strong noise generation. The PF for tone $B^{(1)}$ appears chaotic and without clear noise generation pattern. Rather, it appears that tonal noise at that frequency is being generated throughout the jet flow. This could be an artifact of the methodology given that the intensity of tone $B^{(1)}$ was much weaker those of $B^{(2)}$ or $B^{(3)}$ throughout the scanned region. Strong generation occurs for tone $B^{(2)}$ near the location of the fourth and the fifth shock-cells, and near the second shock-cell for tone $B^{(3)}$.

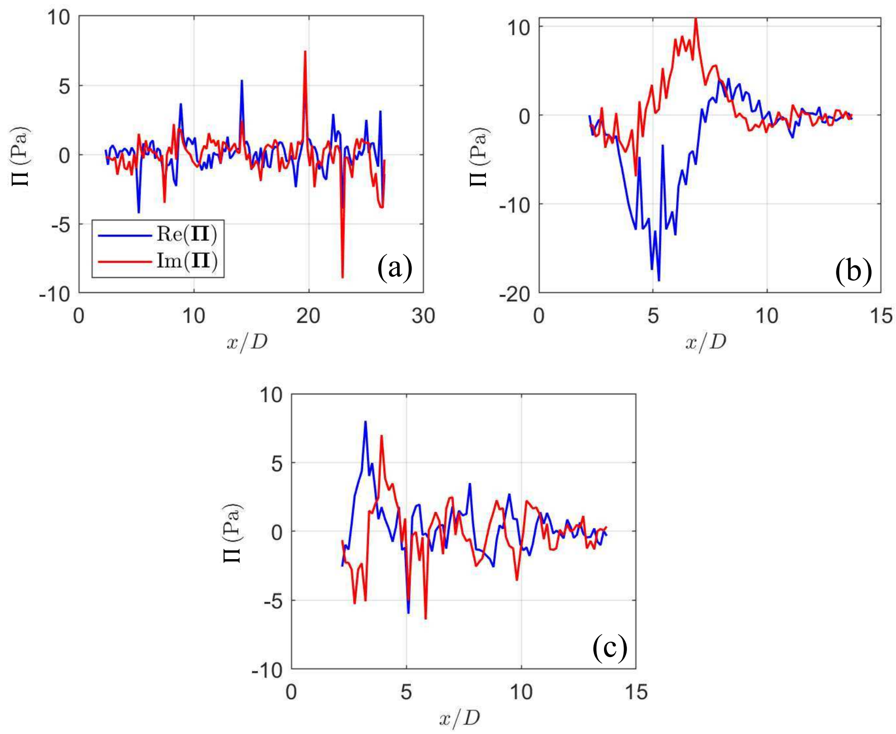


**Fig. 14 Real (blue) and imaginary (red) parts of the partial fields of tones: (a) $B^{(1)}$; (b) $B^{(2)}$; and (c) $B^{(3)}$ for the isolated jet.**

The wavenumber distribution for the partial fields, Eq. 20, is used to determine their non-radiating and radiating components, and the propagation direction of the latter. Figure 15 plots the magnitude of the the radiating part of the partial fields, and their upstream- and downstream-propagating components, for the isolated jet. Only tones $B^{(1)}$, $B^{(2)}$, and $B^{(3)}$ are considered. The main generation for tone $B^{(1)}$ appears to peak near $x/D = 23$, and spreads throughout the the traversed region. This behavior might be attributed to the wide lobes of downstream and upstream radiation pattern of tone $B^{(1)}$ rather than the location of the source itself. Radiation from tone $B^{(2)}$ arises within the third to the fifth shock-cell and then diminishes significantly to virtually zero for $x/D > 10$. The location of the source is in line with previous experimental studies [16, 41] for the same jet. Upstream-propagating waves appear to overtake downstream-propagating waves near $x/D = 5$. Tone $B^{(3)}$ results in intense generation near the second shock cell and from the third to the fifth shock cells, similarly to the pattern of $B^{(2)}$. Here the downstream propagation is stronger than the upstream propagation.

The partial fields obtained for the reflector configuration for tones $E^{(1)}$, $E^{(2)}$ and $F^{(1)}$ are plotted in Fig. 16. The partial field of tone $E^{(1)}$ has a periodic nature that extends to far downstream distances. This might be an indication of stronger oscillation dynamics of mode $E$, which would explain the prominence of tone $E^{(1)}$ over the others. The

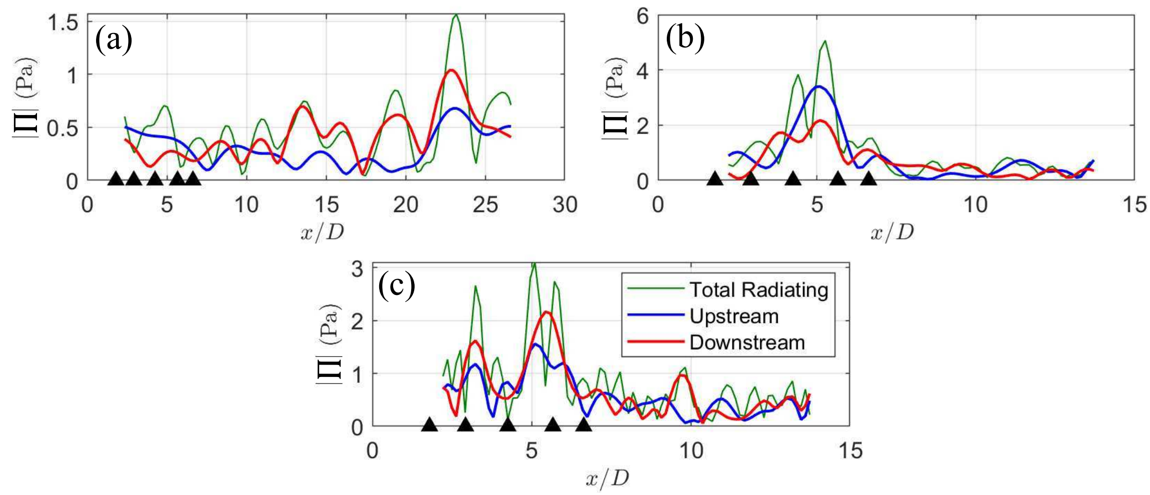


**Fig. 15 Radiating component of the partial fields and its upstream- and downstream-propagating parts for tones: (a) $B^{(1)}$; (b) $B^{(2)}$; and (c) $B^{(3)}$ for the isolated jet. Black triangles denote the locations of the shock-cells.**

generation of tone $E^{(2)}$ appears to be similar to that of $B^{(2)}$ for the isolated jet: it is concentrated around the fourth and fifth shock-cell and almost vanishes for downstream positions greater than $x/D = 10$. The interaction of tones $E^{(1)}$ and $B^{(1)}$ gave rise to tone $F^{(1)}$. Generation appears to be located near $x/D = 4$ to 6, in line with the observations made on the plots displaying the coherence magnitude (Fig. 13).

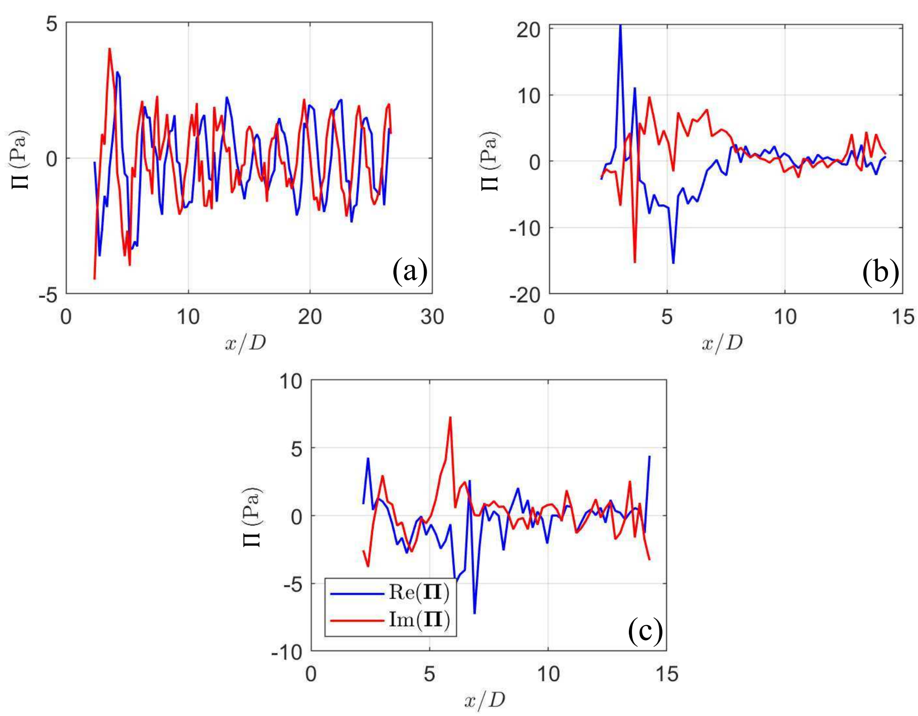


**Fig. 16 Real (blue) and imaginary (red) parts of the partial fields of tones: (a) $E^{(1)}$; (b) $E^{(2)}$; and (c) $F^{(1)}$ for the jet with reflector.**

The contributions from the upstream- and downstream-propagating radiating sources from the reflector case are also separated, in parallel to the previous analysis. They are shown in Fig. 17. It is noted that the total generation of the supersonic components of $E^{(2)}$ and $F^{(1)}$ are relatively similar. However, tone $F^{(1)}$ appears to have stronger downstream-emitting noise generation. The generation for both tones $E^{(2)}$ and $F^{(1)}$ is concentrated between the third and the fifth shock cells. The generation of tone $E^{(1)}$ appears chaotic and distributed over several positions far downstream of the nozzle exit. The peak generation occurs near the fourth and fifth shock-cells and near $x/D = 5$ and 11.

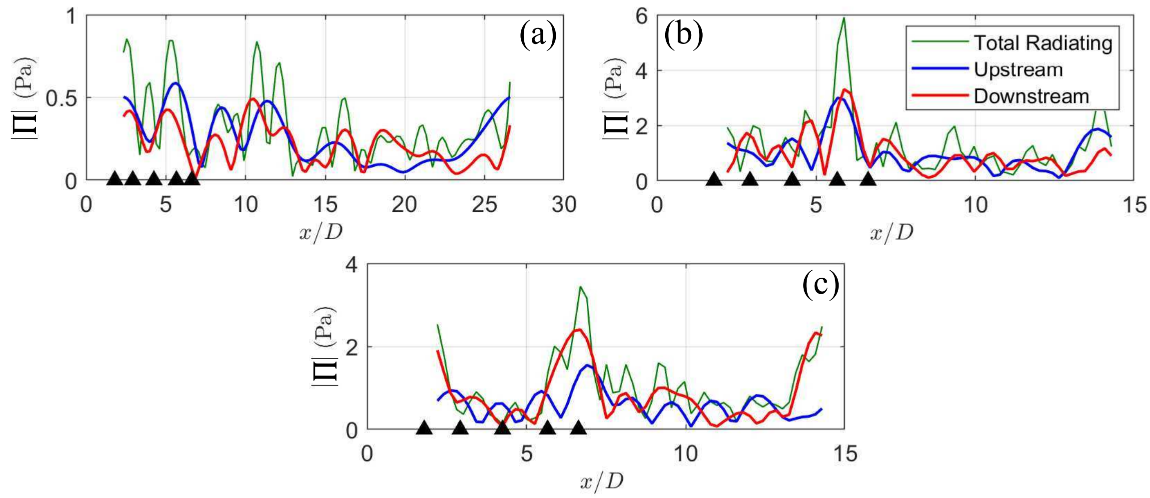


**Fig. 17 Radiating component of the partial fields and its upstream- and downstream-propagating parts for tones: (a) $E^{(1)}$; (b) $E^{(2)}$; and (c) $F^{(1)}$ for the jet with reflector. Black triangles denote the locations of the shock-cells.**

### F. Propagation to Far Field

The surface on which the PFs were imposed was created and meshed using ANSYS with a density of at least 10 elements per acoustic wavelength to prevent resolution errors. The radiating surface extends further upstream and downstream compared to the scanned region (see Fig. 6) to prevent scattering effects. The shape of the radiating surface is shown in Fig. 18. Of the partial fields discussed in Section III.E, those with finite extent within the scanned

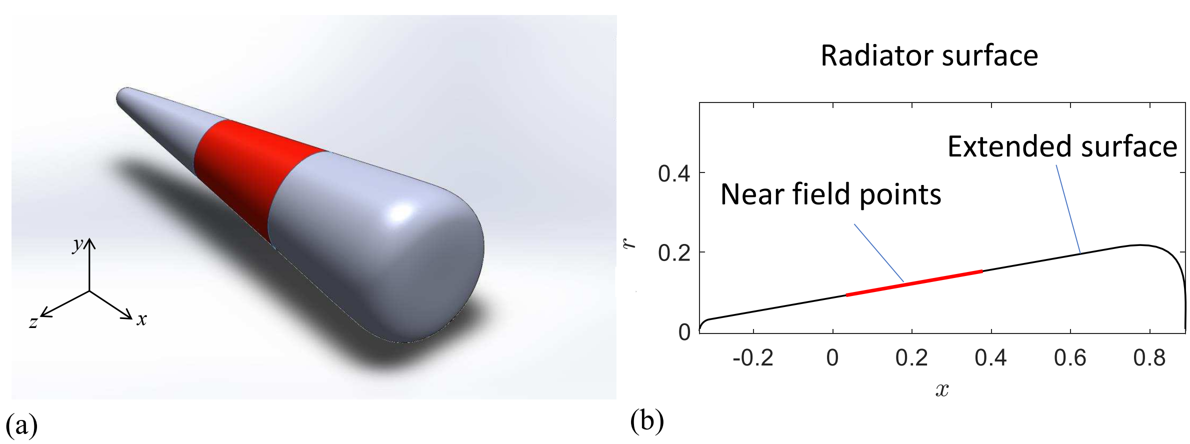


**Fig. 18 Radiator surface used in the BEM. (a) Three-dimensional view, with the active region marked in red; and (b) radial coordinates.**

region were selected for propagation using the BEM. Here we consider the partial fields for tones $B^{(2)}$ (isolated jet) and $E^{(2)}$ (reflector) as shown in Figs. 14b and 16b). In the absence of information on the azimuthal content of the tones, both partial fields are considered axisymmetric. The field points were placed in the far field along the line of experimental microphone measurements for the same jet [41]. The BEM pressure field was converted to sound pressure level (SPL) spectra and comparisons were made with the experimental lossless SPL spectra. Both sets of spectra were processed with $N_{\mathrm{FFT}} = 1024$ and are referenced to a radius of 0.305 m (1 ft) from the nozzle exit.

Figure 19 plots the directivity of the SPL for tones $B^{(2)}$ and $E^{(2)}$ obtained from the BEM (black line) and measured experimentally (red circles). The polar angle $\theta$ is measured from the downstream axis. The plots show reasonable agreement, capturing the directional nature of tone $B^{(2)}$ and the relatively flat emission pattern of tone $E^{(2)}$. The technique is not yet optimized and improvements are possible by including the azimuthal content and refining the block schedule for signal division. The overall agreement shown in Fig. 19 is seen as a promising step towards the development of low-order models, based on linear partial fields, for understanding and predicting the screech feedback loop process.

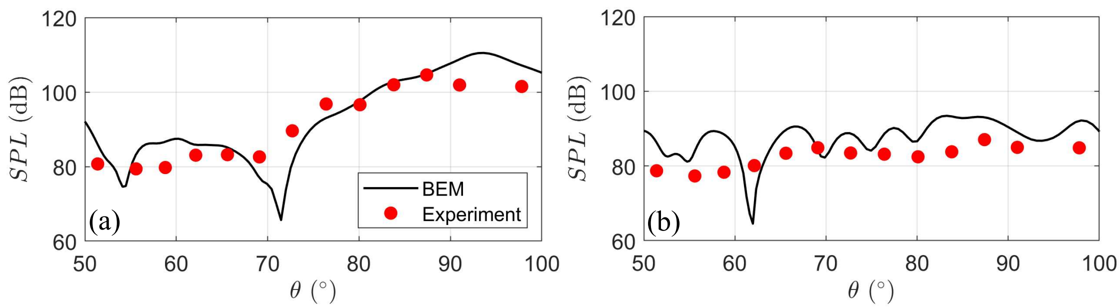


**Fig. 19 Far-field directivity of the SPL predicted from BEM and measured experimentally. (a) Tone $B^{(2)}$ for isolated jet; and (b) tone $E^{(2)}$ for jet with reflector.**

## VI. Conclusions

This study examined experimentally the near-field of an underexpanded supersonic jet and the effect of a conical reflector surface on the space-time emission of screech noise. The supersonic jet issued from a convergent nozzle with a diameter of 14.22 mm at a fully-expanded jet Mach number $M_j = 1.34$. The isolated jet emitted the well-known screech mode $B$, denoting a lateral oscillation. Addition of the reflector caused significant changes in the emission pattern and the near-field statistics, with the emergence of new tones pertaining to mode $E$.

The near-field was surveyed utilizing a microphone phased array that included a continuously-scanning microphone, enabling high spatial resolution in evaluating the statistics of the jet flow field. The processing of the microphone signals involves their division into blocks and the application of the frequency-dependent Gaussian window of Ref. [24]. The fixed microphones are utilized for phase referencing to construct partial fields, which yield a cross-spectral matrix (CSM) based on the locations of the scanning sensor for each block. Traditional beamforming and deconvolution, based on this CSM, were utilized to compute the noise source maps of the two jet flow fields. Peak generation of broadband shock-associated noise (BBSAN) occurs between the fourth and the fifth shock cells. The relative shock strength is used to quantify the differences between the shock-cell patterns of the two jets. The reflector enhances emission from the first four shock cells and increases generation of BBSAN past the fifth shock cell.

Cross-beam forming was used to infer the degree of source coherence. A coherence pattern is detected at the screech tone frequencies between the third, fourth and fifth shock-cells. The pattern is not present for the BBSAN or for frequencies outside the screech tones. The radiating components of the partial fields were analyzed to determine the approximate location of the screech sources. Most of the screech generation is located between the fourth and the fifth shock-cell structures. Finally, the tonal partial fields were propagated to the far field using the boundary element method. The resulting directivity of the sound pressure level spectrum is in fair agreement with experimental results for the same jets, thus highlighting the potential of high-resolution array methods, deployed in the near field, to accurately characterize the jet noise source.

# Acknowledgements

This work was partially supported by NASA Phase II Small Business Innovation Research (SBIR) contract 80NSSC20C0089 under technical monitor Dr. David Stephens of NASA GRC. ATA Engineering, Inc. was the prime. Mr. Andres Adam created and meshed the radiator surface, and propagated the PFs using the BEM software. His work is extremely appreciated. The suggestions by Dr. Parthiv Shah to study the partial fields are greatly appreciated and motivated parts of this study.


# References


[1] Raman, G., "Supersonic Jet Screech: Half-Century from Powell to the Present," *Journal of Sound and Vibration*, Vol. 225, No. 3, 1999, pp. 543–571. doi:10.1006/jsvi.1999.2181.

[2] Manning, T., and Lele, S., "A numerical investigation of sound generation in supersonic jet screech," *AIAA Paper 2000-2081*, 2000. doi:10.2514/6.2000-2081.

[3] Powell, A., "On the Mechanism of Choked Jet Noise," *Proc. Phys. Soc. London*, Vol. 26, 1953, pp. 1039–1056.

[4] Suzuki, T., and Lele, S. K., "Shock Leakage Through an Unsteady Vortex-laden Mixing Layer: Application to Jet Screech," *Journal of Fluid Mechanics*, Vol. 490, 2003, p. 139–167. doi:10.1017/S0022112003005214.

[5] Edgington-Mitchell, D., Weightman, J., Lock, S., Kirby, R., Nair, V., Soria, J., and Honnery, D., "The Generation of Screech Tones by Shock Leakage," *Journal of Fluid Mechanics*, Vol. 908, 2021, p. A46. doi:10.1017/jfm.2020.945.

[6] Tam, C. K. W., Parrish, S. A., and Viswanathan, K., "Harmonics of Jet Screech Tones," *AIAA Journal*, Vol. 52, No. 11, 2014, pp. 2471–2479. doi:10.2514/1.J052850.

[7] Raman, G., "Screech Tones from Rectangular Jets with Spanwise Oblique Shock-Cell Structures," *AIAA Paper 1996-0643*, 1996. doi:10.2514/6.1996-643.

[8] Edgington-Mitchell, D., Weightman, J., Lock, S., Kirby, R., Nair, V., Soria, J., and Honnery, D., "The Generation of Screech Tones by Shock Leakage," *Journal of Fluid Mechanics*, Vol. 908, 2020. doi:10.1017/jfm.2020.945.

[9] Mercier, B., Castelain, T., and Bailly, C., "Experimental Characterisation of the Screech Feedback Loop in Underexpanded Round Jets," *Journal of Fluid Mechanics*, Vol. 824, 2017, p. 202–229. doi:10.1017/jfm.2017.336.

[10] Ponton, M., and Seiner, J., "The effects of nozzle exit lip thickness on plume resonance," *Journal of Sound and Vibration*, Vol. 154, No. 3, 1992, pp. 531–549. doi:10.1016/0022-460X(92)90784-U.

[11] Panda, J., "An experimental investigation of screech noise generation," *Journal of Fluid Mechanics*, Vol. 378, 1999, p. 71–96. doi:10.1017/S0022112098003383.

[12] Raman, G., "Screech Rones from Rectangular Jets with Spanwise Oblique Shock-Cell Structures," *Journal of Fluid Mechanics*, Vol. 330, 1997, p. 141–168. doi:10.1017/S0022112096003801.

[13] Raman, G., "Cessation of Screech in Underexpanded Jets," *Journal of Fluid Mechanics*, Vol. 336, 1997, pp. 69–90. doi:10.1017/S002211209600451X.

[14] Edgington-Mitchell, D., "Aeroacoustic Resonance and Self-Excitation in Screeching and Impinging Supersonic Jets – A Review," *International Journal of Aeroacoustics*, Vol. 18, No. 2-3, 2019, pp. 118–188. doi:10.1177/1475472X19834521.

[15] Islam, M. T. K., and Seto, K., "Control of Supersonic Jet Noise with a Spherical Reflector," *The Journal of the Acoustical Society of America*, Vol. 116, No. 4, 2004, pp. 2539–2540. doi:10.1121/1.4785132.

[16] Morata, D., and Papamoschou, D., "Extension of Traditional Beamforming Methods to the Continuous-Scan Paradigm," *AIAA Paper 2022-1154*, 2022.

[17] Gao, J. H., and Li, X. D., "A Multi-Mode Screech Frequency Prediction Formula for Circular Supersonic Jets," *The Journal of the Acoustical Society of America*, Vol. 127, No. 3, 2010, pp. 1251–1257. doi:10.1121/1.3291001.

[18] Gojon, R., and Bogey, C., "Numerical study of the flow and the near acoustic fields of an underexpanded round free jet generating two screech tones," *International Journal of Aeroacoustics*, Vol. 16, No. 7-8, 2017, pp. 603–625. doi:10.1177/1475472X17727606.

[19] Chakrabarti, S., Gaitonde, D., and Unnikrishnan, S., "Representing Rectangular Jet Dynamics Through Azimuthal Fourier Modes," *Phys. Rev. Fluids*, Vol. 6, 2021, p. 074605. doi:10.1103/PhysRevFluids.6.074605.

[20] Chakrabarti, S., Gaitonde, D. V., and Unnikrishnan, S., "Wavepacket Dynamics in Rectangular Jets," *AIAA Paper 2022-2403*, 2022. doi:10.2514/6.2022-2403.

[21] Stahl, S. L., Prasad, C., and Gaitonde, D. V., "Feedback Mechanisms in a Supersonic Impinging Jet using Conditional Proper Orthogonal Decomposition," *AIAA Paper 2022-1153*, 2022. doi:10.2514/6.2022-1153.

[22] Prasad, A. L. N., Saleh, Y., Sellappan, P., Nair, U. S., and Alvi, F. S., "Near-Field and Far-Field Effects of Heating in an Over-Expanded Mach 2 Diamond Jet," *AIAA Paper 2022-1152*, 2022. doi:10.2514/6.2022-1152.

[23] Shah, P. N., White, A., Hensley, D., Papamoschou, D., and Vold, H., "Continuous-Scan Phased Array Measurement Methods for Turbofan Engine Acoustic Testing," *Journal of Engineering for Gas Turbines and Power*, Vol. 141, No. 8, 2019. doi:10.1115/1.4042395.

[24] Papamoschou, D., Morata, D., and Shah, P., "Inverse Acoustic Methodology for Continuous-Scan Phased Arrays," *AIAA Journal*, Vol. 57, No. 12, 2019, pp. 5126–5141. doi:10.2514/1.J058085.

[25] Morata, D., and Papamoschou, D., "Advances in the Direct Spectral Estimation of Aeroacoustic Sources Using Continuous-Scan Phased Arrays," *AIAA Paper 2021-0215*, 2021. doi:10.2514/6.2021-0215.

[26] Lee, M., and Bolton, J. S., "Scan-Based Near-Field Acoustical Holography and Partial Field Decomposition in the Presence of Noise and Source Level Variation," *The Journal of the Acoustical Society of America*, Vol. 119, No. 1, 2006, pp. 382–393. doi:10.1121/1.2133717.

[27] Lee, M., and Bolton, J. S., "Source Characterization of a Subsonic Jet by Using Near-Field Acoustical Holography," *The Journal of the Acoustical Society of America*, Vol. 121, No. 2, 2007, pp. 967–977. doi:10.1121/1.2404626.

[28] Brooks, T., and Humphreys, W., "A Deconvolution Approach for the Mapping of Acoustic Sources (DAMAS) Determined from Phased Microphone Arrays," *AIAA Paper 2004-2954*, 2004. doi:10.2514/6.2004-2954.

[29] Brooks, T., and Humphreys, W., "Extension of DAMAS Phased Array Processing for Spatial Coherence Determination (DAMAS-C)," *AIAA Paper 2006-2654*, 2006. doi:10.2514/6.2006-2654.

[30] Sijtsma, P., Merino-Martinez, R., Malgoezar, A. M., and Snellen, M., "High-resolution CLEAN-SC: Theory and experimental validation," *International Journal of Aeroacoustics*, Vol. 16, No. 4-5, 2017, pp. 274–298. doi:10.1177/1475472X17713034.

[31] Luesutthiviboon, S., Malgoezar, A. M., Merino-Martinez, R., Snellen, M., Sijtsma, P., and Simons, D. G., "Enhanced HR-CLEAN-SC for resolving multiple closely spaced sound sources," *International Journal of Aeroacoustics*, Vol. 18, No. 4-5, 2019, pp. 392–413. doi:10.1177/1475472X19852938.

[32] Venkatesh, S. R., Polak, D. R., and Narayanan, S., "Beamforming Algorithm for Distributed Source Localization and Its Application to Jet Noise," *AIAA Journal*, Vol. 41, No. 7, 2003, pp. 1238–1246. doi:10.2514/2.2092.

[33] Harker, B. M., Neilsen, T. B., Gee, K. L., Wall, A. T., and James, M. M., "Spatiotemporal-Correlation Analysis of Jet Noise from a High-Performance Military Aircraft," *AIAA Journal*, Vol. 54, No. 5, 2016, pp. 1554–1566. doi:10.2514/1.J054442.

[34] Brooks, T., and Humphreys, W., "Extension of DAMAS Phased Array Processing for Spatial Coherence Determination (DAMAS-C)," *AIAA Paper 2006-2654*, 2006. doi:10.2514/6.2006-2654.

[35] Ravetta, P. A., Burdisso, R. A., and Ng, W. F., "Noise Source Localization and Optimization of Phased-Array Results," *AIAA Journal*, Vol. 47, No. 11, 2009, pp. 2520–2533. doi:10.2514/1.38073.

[36] Ravetta, P. A., Burdisso, R. A., and Ng, W. F., "Noise Source Localization and Optimization of Phased-Array Results," *AIAA Journal*, Vol. 47, No. 11, 2009, pp. 2520–2533. doi:10.2514/1.38073.

[37] Harker, B. M., Gee, K. L., Neilsen, T. B., Wall, A. T., and James, M. M., "Beamforming-Based Wavepacket Model for Noise Environment Predictions of Tactical Aircraft," *AIAA Paper 2017-4048*, 2017. doi:10.2514/6.2017-4048.

[38] Liu, Y. J., "Fast Multipole Boundary Element Method - Theory and Application in Engineering," *Cambridge University Press*, 2009.

[39] Yüceil, K., and Ötügen, M., "Scaling Parameters for Underexpanded Supersonic Jets," *Physics of Fluids 14*, 2002. doi:10.1063/1.1513796.

[40] Seiner, J. M., Manning, J. C., and Ponton, M. K., "Dynamic Pressure Loads Associated with Twin Supersonic Plume Resonance," *AIAA Journal*, Vol. 26, No. 8, 1988, pp. 954–960. doi:10.2514/3.9996.

[41] Morata, D., and Papamoschou, D., "Effect of Nozzle Geometry on the Space-Time Emission of Screech Tones," *AIAA Paper 2021-2306*, 2021. doi:10.2514/6.2021-2306.

[42] Tam, C. K., Parrish, S. A., and Viswanathan, K., "The Harmonics of Jet Screech Tones," *AIAA Paper 2013-2091*, 2013. doi:10.2514/6.2013-2091.

[43] Norum, T. D., "Screech Suppression in Supersonic Jets," *AIAA Journal*, Vol. 21, No. 2, 1983, pp. 235–240. doi:10.2514/3.8059.